Cs3Bi2I9/g-C3N4 as a new binary photocatalyst for efficient visible-light photocatalytic processes

Bresolin Bianca-Maria, Sgarbossa Paolo, Bahnemann Detlef-W., Sillanpää Mika

This is a Final draft version of a publication

published by Elsevier

in Separation and Purification Technology

DOI: 10.1016/j.seppur.2020.117320

Copyright of the original publication: © 2020 Elsevier B.V.

Please cite the publication as follows:

Bresolin, B.-M., Sgarbossa, P., Bahnemann, D.-W., Sillanpää, M. (2020). Cs3Bi2I9/g-C3N4 as a new binary photocatalyst for efficient visible-light photocatalytic processes. Separation and Purification Technology, vol. 251. DOI: 10.1016/j.seppur.2020.117320

This is a parallel published version of an original publication. This version can differ from the original published article.

$Cs_3Bi_2I_9$/g-C_3N_4 as a new binary photocatalyst for efficient visible-light photocatalytic processes

Bianca-Maria Bresolin[a*], Paolo Sgarbossa[b], Detlef W. Bahnemann[c,d,e], Mika Sillanpää [f,g,h]

[a] Laboratory of Green Chemistry, School of Engineering Science, Lappeenranta University of Technology, Sammonkatu 12, 50130 Mikkeli, Finland.
[b] Dipartimento di Ingegneria Industriale, Università di Padova, Via Marzolo 9, 35131 Padova, Italy
[c] Institut für Technische Chemie, Leibniz Universität Hannover, Callinstr. 3, D-30167 Hannover, Germany
[d] Laboratory of Nano- and Quantum-Engineering (LNQE), Gottfried Wilhelm Leibniz University Hannover, Schneiderberg 39, D-30167 Hannover, Germany.
[e] Laboratory ‘‘Photoactive Nanocomposite Materials’’, Saint-Petersburg State University, Ulyanovskaya str. 1, Peterhof, 198504 Saint-Petersburg, Russia
[f] Institute of Research and Development, Duy Tan University, De Nang 550000, Vietnam;
[g] Faculty of Environmental and Chemical Engineering, Duy Tan University, De Nang 550000, Vietnam
[h] School of Civil Engineering and Surveying, Faculty of Health, Engineering and Science, University of Southern Queensland, West Street, Toowoomba 4350, QLD, Australia

Abstract

Recently lead-free halide perovskite have shown great performances, especially in solar cell applications. On the other hand, graphitic carbon nitride g-C_3N_4 *materials have been rising interest thanks to the tunable electronic structure and excellent physicochemical stability, which could serve as an excellent candidate for photocatalytic applications. In our research, we tried to overcome the low charge transportation efficiency and chemical instability anchoring a cesium/bismuth-based perovskite on g-*C_3N_4 *nanosheets to prepare composite photocatalyst based on nitrogen-iodine chemical bonding. Among different lead-free halide perovskite loads, the CNCSBI001 composite (g-*C_3N_4:$Cs_3Bi_2I_9$ *10:0.1 w%) showed the better stability and an outstanding yield for photocatalytic degradation of organic compound in water solution under visible light irradiation. Hydrogen evolution test were also perform to test the activity of the synthesized compound under simulated solar light irradiation. The former study aim to provide insights on the use of halide perovskite-based Z-scheme photocatalyst for different photocatalytic applications.*

Keywords

Perovskite, Photocatalysis, Lead-free halide perovskite, Visible light

*Corresponding author at: Laboratory of Green Chemistry, School of Engineering Science, Lappeenranta University of Technology, Sammonkatu 12, 50130 Mikkeli, Finland. E-mail address:Biancabresolin@yahoo, Bianca-maria.Bresolin@lut.fi.

1. INTRODUCTION

In the last centuries, the rapid development of urbanization and industrialization have led to two significant issues: an increase of global energy demand and a remarkable release of toxic and harmful chemical pollutants into the environment. To date, scientist have put enormous efforts to advance in sustainable and clean energy technologies to solve the aforementioned crises [1–5].

Among different technologies, photocatalytic processes over semiconductor surfaces have attracted particular attention in recent years as potentially efficient, environmentally friendly and low cost methods for environment remediation [6–9] as well as for renewable hydrogen production [8,10–12].

Light can be considered an ideal reagent for ‘green’ chemical processes due to its non-toxicity, it does not produce any waste, and it can be obtained from renewable sources. For this reason solar energy has attracted much interest because it is the most abundant and clean source of energy, thus built artificial photosynthetic systems able to convert solar energy into chemical energy may be desirable.

Recently, graphitic carbon nitride (g-C_3N_4) has been worldwide labelled as a suitable candidate to be investigated as a potential next-generation materials for sustainable energy conversion and catalyst applications [13–15]. Among the advantageous properties of the g-C_3N_4 nanostructures one can mention: the high surface area, the quantum efficiency, the separation and transport of the interfacial charge and the ease of modification through the formation of composites or the incorporation of surface functional groups [16]. Considering these outstanding features, there is a remarkable scientific effort seeking to couple it with other semiconductors to fabricate nanocomposites with excellent photocatalytic performance toward environmental remediation by improving charge carrier separation and transportation, prolonging the charge carrier lifetime, enlarging specific surface area and enhancing adsorption sites.

Recently, halide perovskite materials have attracted remarkable interest in particular in photovoltaics and optoelectronic applications due to their unique efficiency. Some of the remarkable properties that make these materials promising candidates for photocatalytic applications are large absorption coefficients due to the favourable band gap, point defects, grain boundary and long electron–hole diffusion length that reduced electron-hole pair recombination [17]. Moreover, the synthesis of these materials is easily reproducible and low cost. In the past, lead halide perovskite showed the better efficiency as harvester of solar energy [18–23]. Unfortunately, this material showed instability especially in high humidity, the possible leaching of Pb^{2+} as bioavailable cation, make the lead-based material toxic and unsuitable especially for wastewater treatment. On contrary, bismuth-based perovskites promise good moisture and water stability [18,24–26].

In recent years, lead based halide perovskite/carbon based-materials such as graphene oxide or g-C_3N_4 composites were found to be particularly active for photocatalytic CO_2 reduction [23,27]. Built up composite photocatalysts by anchoring semiconductor-materials on g-C_3N_4 is based on some important considerations. The band alignment between the interfaces of materials can facilitate charge separation and transportation [28,29]. Secondly, g-C_3N_4 surface functionalization may enhance the interaction of particles with other materials. Thus, amino or carboxyl groups can perform strong chemical interactions stronger than physical adsorption. Moreover, the halide perovskite particles passivated by the graphitic carbon nitride surface is expected to be more stable in photoreaction [30,31]. This can be address to overcome instability towards water that is a challenge for common practical applications of halide perovskites.

So far, for fabrication of efficient modified photocatalysts, different strategies have been employed, especially, they have been addressed to increase the visible-light activity. Among them, much efforts have been spent in heterojunction construction and coupling synthesis of bismuth based nano-materials, but their potential has still to be thoroughly explored. Even though major advancements have been made to improve photocatalytic activity of Bi-based photocatalysts more efforts are still necessary [32].

In our work, we investigate a new potential composite photocatalyst g-C_3N_4:$Cs_3Bi_2I_9$ for photocatalytic applications under visible light irradiation. Herein, we report a facile self-assembly synthesis of a g-C_3N_4:$Cs_3Bi_2I_9$ heterogeneous photocatalyst through their electrostatic interactions that facilitate the spontaneous assembly of the two charged components.

To the best of our knowledge, this is the first time that a g-C_3N_4:$Cs_3Bi_2I_9$ hybrid structure is prepared and tested in photocatalytic application under visible light irradiation.

2. MATERIALS AND METHODS

2.1 Materials

All chemicals including dicyandiamide (99%), melamine (99%), Urea (>99.5%), CsI (99.999%), BiI_3 (99%), N,N-dimethylformamide (DMF, anhydrous, 99.8%) were purchased from Sigma-Aldrich and used without further purification. Deionized water was used during the preparation.

2.1.1. Preparation of $Cs_3Bi_2I_9$

The synthesis method of $Cs_3Bi_2I_9$ is consistent with previous report [25]. Briefly, BiI_3 and CsI were mixed (2:3 molar ration) into a round bottom flask in DMF. The mixture was heated at 60 ^{o}C under magnetic stirring to the total evaporation of the solvent. Subsequently, the solid was washed three times with diethyl ether and water, dried to remove the residue of DMF. A shining red powder was obtained and kept in dark for further use. The elemental analysis of the dried sample indicated that very low C and N contents (2.1 wt% and 1.6 wt% respectively) were remaining in the final sample, implying that solvent molecules were largely removed.

2.1.2. Preparation of g-C_3N_4

The g-C_3N_4 was synthesized according to previous reports [33,34]. In general, g-C_3N_4 can be readily fabricated through a traditional thermal condensation. Different low-cost N-rich organic solid precursors can be used, such as urea, thiourea, melamine, dicyandiamide or cyanamide at 500–600◦C in air or inert atmosphere. Herein, g-C_3N_4 was prepared by heating directly in ceramic crucible. Briefly, the precursor was calcined for 2 h at 550 °C in a covered ceramic crucible. The U/ g-C_3N_4, M/ g-C_3N_4 and D/ g-C_3N_4 were prepared as reported with urea, melamine or dicyanamide as precursors, respectively. All the yellow products were weighted before and after to measure the synthesis yield (**Table 1**).

The yields were evaluated to compare the efficiencies of the synthesis as optimization parameter. Thus, melamine was selected as precursor due to its higher synthesis yield.

Table 1: *g-C_3N_4 synthesis yield*

precursor	temperature °C / time h	name	yield $w_{final}/w_{initial}$ (%)
urea	550 / 4	U/g-C_3N_4	9.2
melamine	550 / 4	M/g-C_3N_4	54.6
dicyanamide	550 / 4	D/g-C_3N_4	52.6

2.1.3. Preparation of $Cs_3Bi_2I_9$:g-C_3N_4

Approximately 10g of g-C_3N_4 powder were dispersed in an appropriate amount of hexane and ultra-sonicated for 15 min. Then, a certain percentage of $Cs_3Bi_2I_9$ was added to the suspension and ultra-sonicated for 30 minutes. Finally, the composites were obtained after centrifugation at 6000 rpm for 5 min followed by drying at 40 °C. The weight percentage of $Cs_3Bi_2I_9$ with respect to g-C_3N_4 was either 1 or 10 wt%, the corresponding sample is denoted as CNCSBI001 or CNCSBI01, respectively. The scheme of synthesis is shown in **Figure 1.**

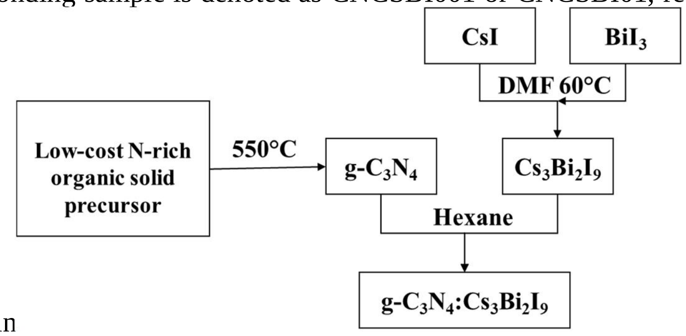

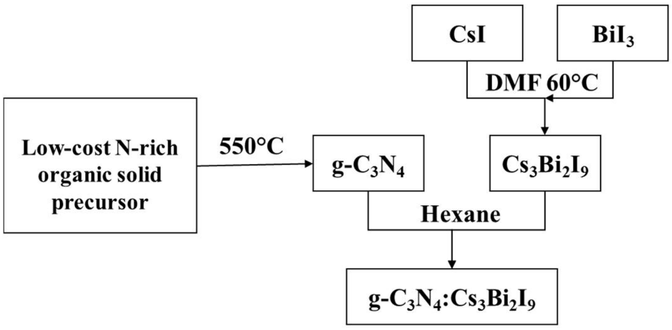

Figure 1: *Schematic illustration for the synthesis of the photocatalyst*

2.2 Characterization of the photocatalyst

2.2.1. Structural characterization

Diffuse reflectance spectra were recorded using a Cary 4000 spectrophotometer (Varian). XRD spectra of samples were collected using a PANalytical θ/θ diffractometer (CuKα radiation; 40 kV and 40 mA). The transmission IR spectra of the samples in KBr pellets are recorded on a Perkin-Elmer Spectrum 100 FTIR spectrophotometer in the region 400-4000 cm^{-1}. Environmental scanning electron microscopy measurements were performed on Philips XL, 30-XRF-EDS embedded. Transmission electron microscopy analysis were performed with TECNAI FEI G2 microscope.

2.2.2. Photoelectrochemical measurements

The electrochemical and photoelectrochemical measurements were performed using a Zennium potentiostat and a PECC-2 photoelectrochemical cell (Zahner-Elektrik GmbH & Co. KG). The standard three-compartment cell used consisted of the working electrode, a Pt wire counter electrode and an Ag/AgCl reference electrode. 0.1 M Na_2SO_4 was used as electrolyte solution at pH 7. The working electrode was prepared using doctor blade technique, annealed at 400 °C for 2 h in order to remove organic chemicals. Mott–Schottky measurements were performed at a frequency of 100 Hz and 5 mV of amplitude. During the polarization measurements the illumination source was chopped on and off with a frequency of 250 mHz. The light source was a solar simulator with a 300 W, 678 Wm^{-2} Xenon lamp (LOT-Quantum Design GmbH) and an AM-1.5 G filter. IPCE, Incident photon to current conversion efficiency measurements, were carried out using a white LED (TLS, Zahner) coupled with a USB controlled monochromator in a wavelength range of 430–730 nm.

2.3 Photocatalytic application tests

2.3.1 Aqueous phase organic contaminant degradation

Initially, visible-light photocatalytic efficiency was investigated and compared on the treatment of some well known organic contaminants: Rhodamin B (RhB), Methylene Blue (MB), Methyl Orange (MO), and a mix of organic dyes simultaneously (MB and MO). In general, 0.5 g/L of the photocatalyst was suspended in 100 mL of aqueous solution containing different amount of organic contaminant. The suspension was maintained in dark condition for 60 minutes in order to reach the adsorption–desorption equilibrium. Afterwards, the suspension was irradiated using a **LED-visible light lamp** (A passively cooled VisiLight LED3 was used. The lamp assure environmentally friendly LED technology with flicker free illumination, 36W power consumption, 730 lm luminous intensity). During the photocatalytic tests, 3 mL of the sample was taken at given time intervals and filtered to separate the catalyst (0.2µm). The degradation results were monitored using a UV/vis spectrometer (Lambda 25, Perkin Elemer). As well known, dyes absorb visible-light photons (dye sensitization), thus photoexcited electrons may be injected into photocatalyst particles enhancing the photocatalytic activity. For further testing the photocatalytic activity of the as synthesized composite, methanol (MeOH) oxidation was evaluated. In a typical experiment, 1 g/L of catalyst was added in 75 mL of MeOH aqueous solution (100 mM). The suspension was stirred in the dark for 30 min to reach the adsorption–desorption equilibrium. During the photocatalytic tests, performed under **LED visible-lamp irradiation** (M455L3-455 nm, ThorLABS), 0.5 mL of the sample were taken at given time intervals and separated by filtration (0.2µm) to remove the catalyst. The degradation of methanol was evaluated using the Hantzsch reaction with subsequent fluorescence analysis to quantify the amount of formaldehyde produced in an aqueous solution. This method, known as the Nash method, is widely used to determine formaldehyde concentrations. In brief, formaldehyde condenses with acetylacetone in the presence of an ammonium acetate as buffer, according to the Hantzsch reaction, to form 3,5-diacetyl-1,4-dihydrolutidin (DDL). The former compound is fluorescence active and shows a band at 510 nm when excited at 405 nm. The fluorescence of DDL was measured in a well plate (Nunclon Delta Surface, Thermo Fisher Scientific Inc., USA) sample holder using a UV-visible spectrophotometer, 100 Bio, Cary.

2.3.2 Hydrogen evolution

The prepared photocatalyst with Platinum deposit was used to conduct molecular hydrogen evolution photocatalysis under UV light irradiation (355 nm). The photo-deposition technique was applied to deposit 1 wt % platinum (Pt) on the samples. Hexachloroplatinic acid (H_2PtCl_6 $6H_2O$) was used as the Pt precursor, methanol was used as a reducing agent (10 vol/vol. % in water). The suspension was transferred into a closed reactor and placed under UV-light for 12 h with continuous stirring. The suspension was washed several times with water and subsequently with ethanol to remove non-deposited Pt. The sample was finally dried in an oven for 12 h at 90 °C.

In a typical experimental run, 6 mg of the photocatalyst were added into 6 mL of MeOH solution (10 vol%) used as a hole scavenger in a reactor of 12 mL. The suspension inside the photoreactor was degassed for

15 min with Ar to remove air, stirred for 30 min in the dark. Afterwards, the photoreactor was kept under 450 W Xe lamp equipped with a water-filter and aWG320-filter to block UV-B and UV-C. Samples were withdrawn at intervals of one hour. The spectral irradiance measured by a SprectraRad (BWTEK) irradiance meter is shown in **Figure 2**. The increasing hydrogen content was measured hourly by using a gas chromatograph (Shimadzu 8A, Kyoto, Japan) equipped with a TCD detector and a 5 Å molecular sieve packed column. Along the experiments, Ar was used as the carrier gas.

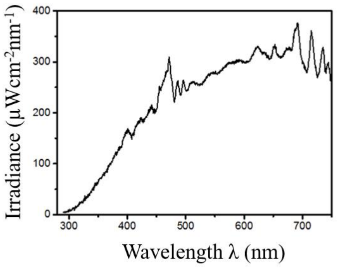

Figure 2*: Irradiance spectrum of the Xe lamp employed in the* H_2 *evolution measurements*

3. RESULTS AND DISCUSSION

3.1 Catalyst characterization

Transmission electron microscope (TEM) and environmental scanning electron microscope (ESEM) images confirmed the successful synthesis of the composite photocatalysts and they are presented in **Figure 3**.

To obtain an understanding of the interfacial interaction between g-C_3N_4 and halide perovskite, the material was characterized by TEM. The layered structure of g-C_3N_4 and the hexagonal structure type of $Cs_3Bi_2I_9$ were both confirmed. The $Cs_3Bi_2I_9$ particles of 45-50 nm in average size have relatively smooth surfaces which become rougher after the anchoring to the g-C_2N_4 sheets (**Figure 3 A1-A3**). The TEM picture of **Figure 3 A1-A3** show different lattice fringes of the as synthesized halide perovskite and the g-C_2N_4 sheet, revealing the formation of the composite after the as performed synthesis. Moreover, TEM images confirmed that the composites exhibit similar morphology with that of bare g-C_3N_4 nanosheets, indicating the structure of g-C_3N_4 remains unchanged after the solvent treatment.

The ESEM images (**Figure 3B**) reveal some important information. First, they confirm the presence of the two material, the lighter particles with higher molecular weights ($Cs_3Bi_2I_9$) and lower (g-C_2N_4) in darker colors. The photographs of g-C_3N_4 and the as prepared material are shown in **Figure 3C**. It can be seen that the color of original g-C_3N_4 is light yellow. However, after compositition with the $Cs_3Bi_2I_9$ perovskite, the as-prepared CNCSBI001 to CNCSBI01 samples turn purple. This is consistent with the success of the synthesis.

EDS analysis confirm the nature of the darker material, mainly composed by C and N, as g-C_2N_4. On the contrary, by the punctual analysis on lighter spots the presence of the $Cs_3Bi_2I_9$ was established. The elemental analysis are reported for the two material in **Figure 3 D1 and D2**, g-C_3N_4 and $Cs_3Bi_2I_9$, respectively. Secondly, the images clearly show the difference in between CNCSBI001 (**Figure 3 B1**) and CNCSBI01 (**Figure 3 B2**) in term of halide perovskite content, 1 and 10%, respectively.

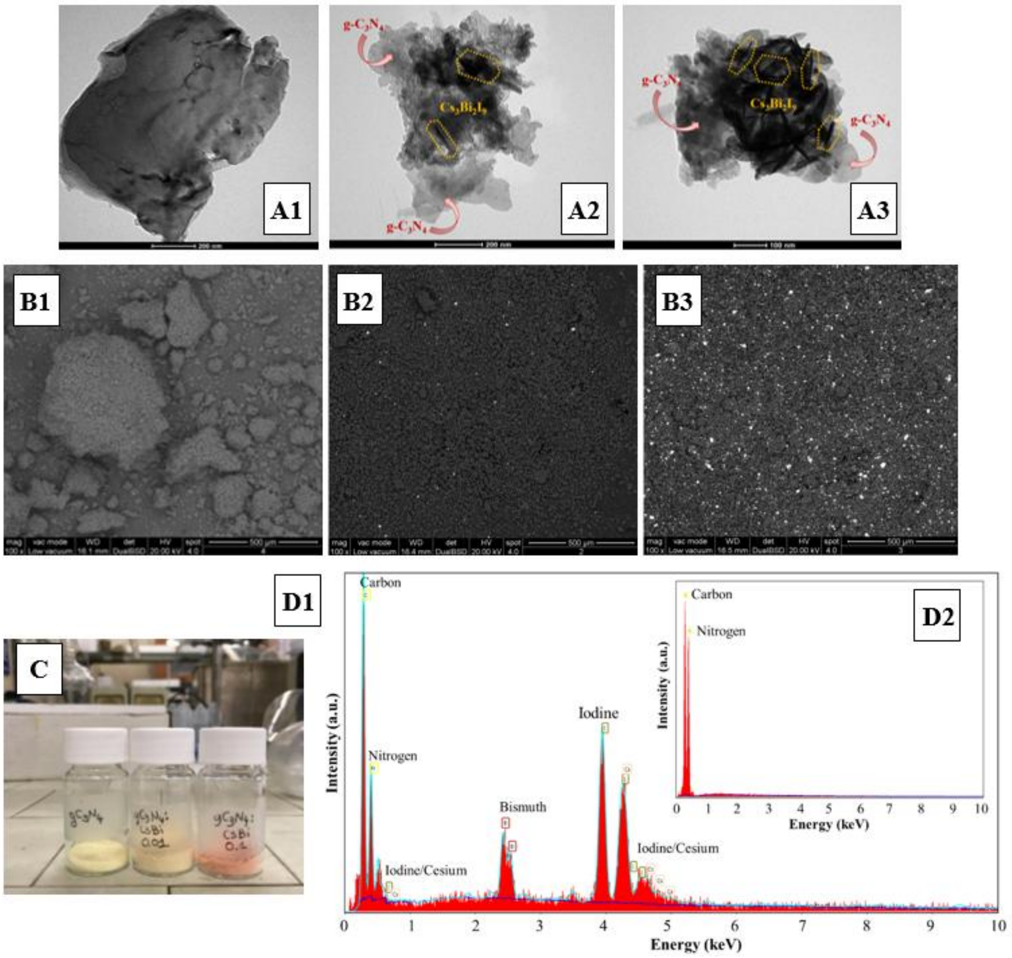

Figure 3: A1) TEM image of g-C_3N_4, **A2)** CNCSBI001 and **A3)** CNCSBI01; **B1)** ESEM images of g-C_3N_4, **B2)** CNCSBI001 and **B3)** CNCSBI01; **C)** photograph of g-C_3N_4, CNCSBI001 and CNCSBI01; **D1)** EDS analysis CNCSBI001; **D2)** EDS analysis g-C_3N_4

XRD measurements reveal the detailed information on the purity and crystallinity of the samples. **Figure 4** shows the XRD patterns of the g-C_3N_4, $Cs_3Bi_2I_9$ and the composites in different molar ratios. All the samples were found to be well crystallized. The peaks of g-C_3N_4 could be well indexed to reference (JCPDS 87-1526) [35]. Two distinct diffraction peaks at 12.99 and 27.80 and can be assigned to the corresponding (100) and (002) diffraction planes of the graphitic carbon nitride. The XRD pattern of $Cs_3Bi_2I_9$ shows that all the peaks are well indexed to the orthorhombic hexagonal crystallographic phase with space group P63/mmc (194) and good crystallinity [25,36]. Moreover, **Figure 4** shows that diffraction peaks of both the halide perovskite and graphitic carbon nitride can be clearly identified in the heterojunction-based photocatalysts and the peak intensities of halide perovskite increase according to its content, 1 and 10%, respectively. The narrow sharp peaks suggest that the products are well crystallized. No impurity peaks were observed, which implies that the two materials were in pure phases in the composites.

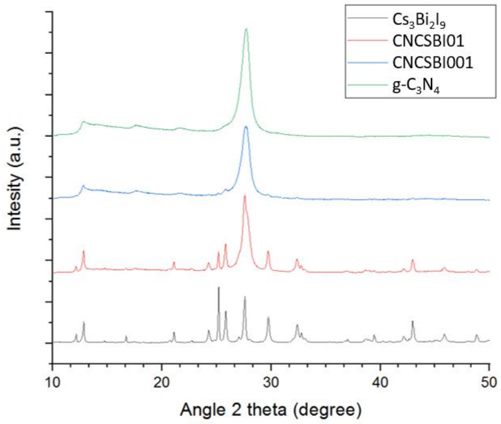

Figure 4: *XRD patterns of g-C_3N_4, CNCsBi001, CNCsBi01 and $Cs_3Bi_2I_9$*

Figure 5A displays the FTIR spectra of the as synthesized materials in order to investigate their chemical bonding and understand the nature of interaction between the two materials. The characteristic vibration peak of the pure graphitic carbon nitride appears at 808, 1245, 1322, 1574, and 1633 cm^{-1}. The peak at 808 cm^{-1} can be assigned to the triazine units, while those from 1245 to 1574 cm^{-1} the stretching vibration of C–N heterocycles. The peaks at 1322 cm^{-1} and 1633 cm^{-1} define the stretching mode of C–N and C=N bonds, respectively. The absorption band ranges between 3000 and 3500 cm^{-1} shows the presence of chemical groups such as NH_x and OH. The absorption intensity in this range is slightly reduced when the perovskite was added to the system due to the substitutional chemical bonds between the two materials. All the FTIR spectra exhibit the characteristic peaks of g-C_3N_4 meaning that no impurity or solvent residue absorption peaks were detected. Moreover, a zoom of the FTIR spectra from 1150 cm^{-1} to 1330 cm^{-1} shows systematically shifted of values with the introducing of lead-free perovskite in the graphitic carbon nitride framework **(Figure 5B)**. The absorption band ranges between 1000 cm^{-1} and 1300 cm^{-1} can be assigned to the aromatic plane C-H bending [37–40]. Furthermore, the ranges between 1400 cm^{-1} and 1600 cm^{-1} belong to C=C and C-C bond from aromatic rings [41,42]. This can be due to the chemical interactions between $Cs_3Bi_2I_9$ and the surface of g-C_3N_4 that increase the electron density of aromatic heterocycles. This can be considered an indication of bonding between the surface functional groups of the graphitic carbon nitride and the lead-free halide perovskite.

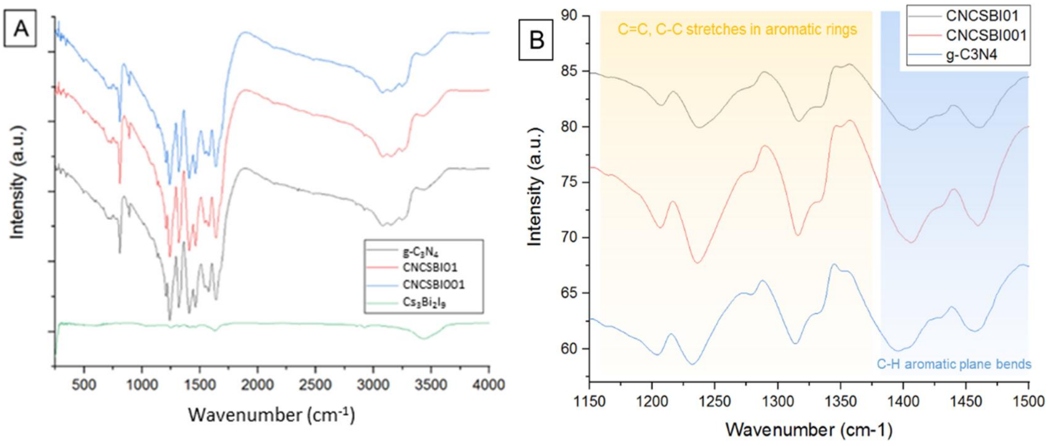

Figure 5: A) *FTIR spectra of g-C_3N_4, CNCsBi001, CNCsBi01 and $Cs_3Bi_2I_9$;* ***B)*** *Zoom on specific regions of FTIR spectra of g-C_3N_4, CNCsBi001, CNCsBi01*

In order to understand the influence of $Cs_3Bi_2I_9$ perovskite nanoparticles on the surface of g-C_3N_4 nanosheets and to investigate the effect of the photocatalytic activity of the heterojunction, the BET surface area of bare g-C_3N_4 and the heterojunctions have been investigated. The BET surface area of the as synthesized materials are 6.30, 15.06 and 17.61 m^2g^{-1} for g-C_3N_4, CNCSBI001 and CNCSBI01, respectively. The surface area measured for the bare $Cs_3Bi_2I_9$ was found to be 10 times lower. However, upon coupling of g-C_3N_4 nanosheets with the lead-free halide perovskite, the BET surface area of the resulting composites was enhanced. It can be assumed that, the increase in surface area may be induced by the exfoliation of g-C_3N_4 in presence of perovskite material and during the ultrasonication process adopted in the synthesis. Thus, the high surface area of the photocatalysts synthesized can provide more reaction sites for the adsorption and degradation of pollutant molecules resulting in the enhancement of photocatalytic ability [43].

Two important parameters of the electronic structure that may affect the photocatalytic activity of semiconductors are the band gap that determine the photons absorption capacity and the flat band potential that affects the recombination probability. For the sake of understanding the mechanism of the electrocatalytic enhancement of the as synthesized heterojunctions DRS and Mott-Schottky measurements were conducted.

Figure 6A shows the absorption spectra of the as synthesized materials in the range of 350-800 nm. The results for the bare g-C_3N_4 exhibited an absorption edge around 470 nm. The pure $Cs_3Bi_2I_9$ has a higher light absorption capacity in the visible region with a band edge around 600 nm. Compared to the pure g-C_3N_4, all the composites exhibit a red shift and a shoulder on the adsorption edge that means an increase in absorption in the visible region. The g-C_3N_4 and $Cs_3Bi_2I_9$ absorption edge can be clearly noticed in CNCSBI01. As expected, a significant increase light absorption intensity in the visible light can be related to the presence of the lead-free halide perovskite, $Cs_3Bi_2I_9$. The band gap was determined by the following equation:

$$\alpha h\nu = A\,(h\nu - Eg)^{n/2}$$

Where α is the optical absorption coefficient, h is the Plank constant, ν is the light frequency, Eg is the band gap, and A is a constant. Both g-C_3N_4 and $Cs_3Bi_2I_9$ possess indirect transition band gaps [25,44,45], thus n is assigned accordingly. By extrapolating the straight line to the x-axis in this plot, the Eg of g-C_3N_4 and $Cs_3Bi_2I_9$ were estimated to be about 2.68 eV and 1.88 eV (as shown in **Figure 6B**), respectively. The two material edges are clearly observed in the measurement performed on CNCSBI001 and CNCSBI01. It is important to mention that in general, the total absorption of the composite can be linked to an increases in the production of electron–hole pairs, resulting in a higher photocatalytic activity.

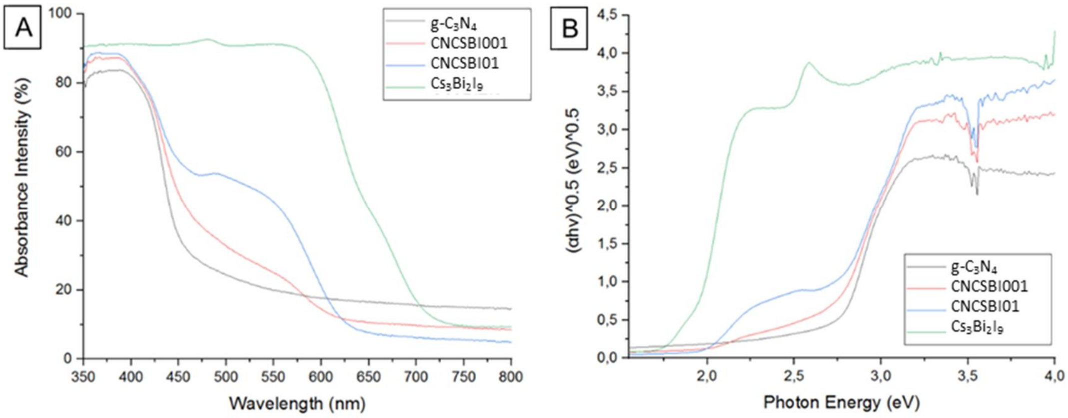

Figure 6: *UV–vis absorption spectra of $Cs_3Bi_2I_9$, CNCSBI001, CNCSBI01 and g-C_3N_4*

It is well known that semiconductors with unique band gap structure may have photoelectric properties that could convert light energy electricity**. Figure 7A** shows the Mott-Schottky plots for the as synthesized materials. The measured area of the electrode is 1.0 cm^2. As expected, all of the plots show a positive slope, meaning that all of the material-based electrodes were *n*-type semiconductors with electrons as the majority carriers. The intersection points of the potential and linear potential curves give the value of the flat band potential (V_{fb}), which are approximately −1.21 V, −1.61 V and -1.79 V versus Ag/AgCl for the graphitic carbon nitride, the heterojunctions and the bare perovskite, respectively. From the results it is theoretically expected that the as prepared heterojunctions may has a relatively stronger reduction ability, due to the negative shift of V_{fb}.

In order to investigate the photoactivity of the samples as a function of wavelength, IPCE (%) measurements were performed under illumination by an AM 1.5 G solar simulator. The results are shown in **Figure 7B**.

Compared with a negligible IPCE obtained for the pure g-C_3N_4, a remarkably increased IPCE was observed for all the materials, with a maximum of 28% around 330 nm for CNCSBI01. On the basis of these findings, increased light absorption may not be the only reason for the improved IPCE, and the contribution of heterojunction effect needs also to be considered.

Figure 7C shows the measured polarization curves of the as synthesized samples under chopped light illumination: g-C_3N_4 (red), CNCSBI01 (purple), CNCSBI001 (blue) and $Cs_3Bi_2I_9$ (grey). All the materials show anodic photocurrent, revealing an n-type response. In all cases, the photocurrent increases with the applied potential. The photoresponse of the samples increases with the content of lead-free halide perovskite. Thus, it is reasonable to conclude that the enhancement of photocurrent measured can be mainly attributed to the presence of perovskite.

The improved charge carrier separation in the photocatalyst was investigated by EIS measurements confirming the effect on the kinetics of interfacial charge transfer between the two materials. The Nyquist plot the smaller arc radius corresponds to a lower charge transfer resistance, thus a better transfer capability. As shown in In **Figure 7D,** the Nyquist plots of the as synthesized heterojunctions CNCSBI001 and CNCSBI01 shown smaller arc radius. A lower value of resistance leads to higher efficiency in charge transfer across the electrode/electrolyte interface. In these cases the charge recombination is reduced respect the bare g-C_3N_4, thus the photocurrent response is higher. The reason for the more efficient charge transport could be the electron–phonon interaction of the two connected materials. The junction between two material can lead to an increase in charge mobility.

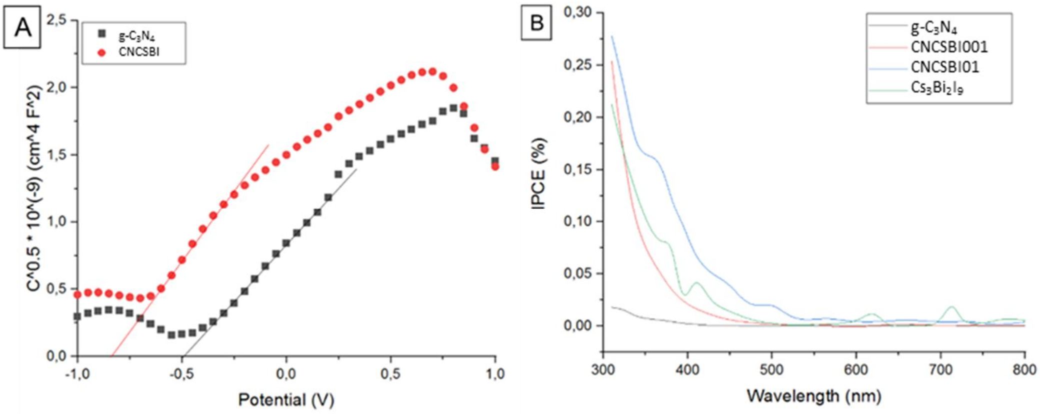

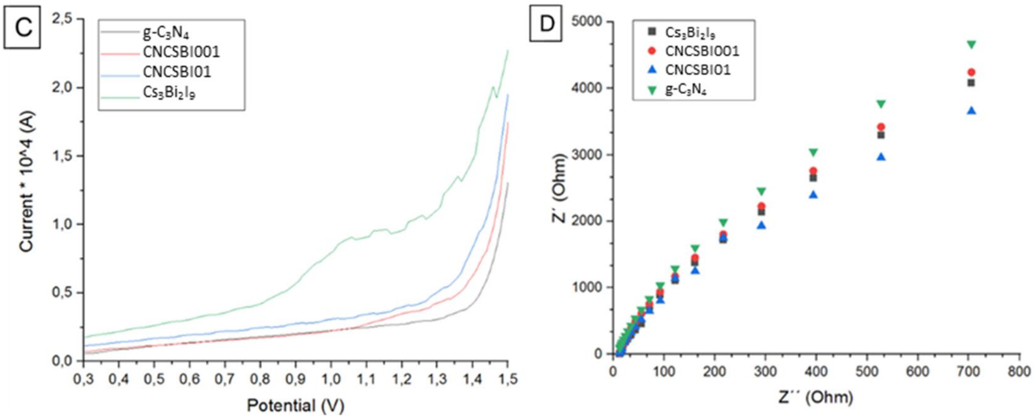

Figure 7: A) Mott-Schottky analysis based on capacitance-voltage measurements for the samples. **B)** Incident photons to current efficiency for photoanodes recorded at a bias of 1.23 V vs. RHE for g-C_3N_4, CNCSBI001, CNCSBI01, $Cs_3Bi_2I_9$. **C)** Polarization curves for g-C_3N_4, CNCSBI001, CNCSBI01, $Cs_3Bi_2I_9$ measured under 250 mHz chopped light illumination (under illumination by an AM 1.5 G solar simulator). **D)** Nyquist plots for g-C_3N_4, CNCSBI001, CNCSBI01, $Cs_3Bi_2I_9$.

3.2 Performance of Photocatalysis

Photocatalytic performance of the as synthesized materials were tested in comparison with the pure precursors, respectively $Cs_3Bi_2I_9$ and g-C_3N_4. The photocatalytic activities of g-C_3N_4/$Cs_3Bi_2I_9$ were measured by the degradation of different organic dyes in water solution under LED-visible light irradiation. Initially, the comparative photocatalytic performance of the as synthesized materials was tested on RhB as probe-dye as a function of irradiation time. In **Figure 8A** can be clearly seen that the CNCSBI001 has the higher efficiency respect the other materials, reaching about 100% of degradation after 120 minutes of visible-light irradiation. The adsorption ability of the as prepared photocatalysts in dark experiments was also investigated. In all cases, it is clearly noted a remarkable enhance of the oxidation rate of the target pollutant as the light was switch on. Initial adsorption experiments conducted in dark for 30 minutes demonstrated the adsorption on the surface of the material is minimal and could be neglected under irradiation conditions. When a higher amount of perovskite was loaded, the lower RhB degradation rate can be ascribed to charge recombination at the excessive defect sites on the surface of material taht not coordinated to g-C_3N_4. The efficiency of photocatalytic activity of the photocatalyst was observed for a wide range of pollutants. **Figure 8B** and **C** shows time-dependent photocatalytic degradation of MB (10 mgL^{-1}), and MO (30 mgL^{-1}), respectively, using a load of 1 gL^{-1} of the as prepared photocatalyst under LED-visible light irradiation. The figures show a total degradation of MB in 180 minutes and a partial degradation of MO in 300 minutes. A higher efficiency in MB degradation can be correlated with the type of available catalytic sites and the binding affinity of the substrates towards the selected organic dye. The results confirmed the photocatalytic ability of the material on the degradation of different types of organic dyes under visible-light irradiation. Finally, a mixture of dyes was used to investigate the photocatalytic efficiency of the as synthesized photocatalyst in complex systems. The maximum absorbance values of the chosen organic dyes do not change upon their mixing, allowing the simultaneous detection of the two contaminants [49,50]. **Figure 8D** shows time-dependent photocatalytic degradation of MB (10 mgL^{-1}) and MO (5 mgL^{-1}) mixed in water solution. From the results, it was concluded that the mixture of the two organic dyes can be degraded effectively using the as synthesized material under visible-light irradiation in presence. The as described investigation was performed because the real dyes originating from various industries typically consist of mixture of contaminants along with interfering substances.

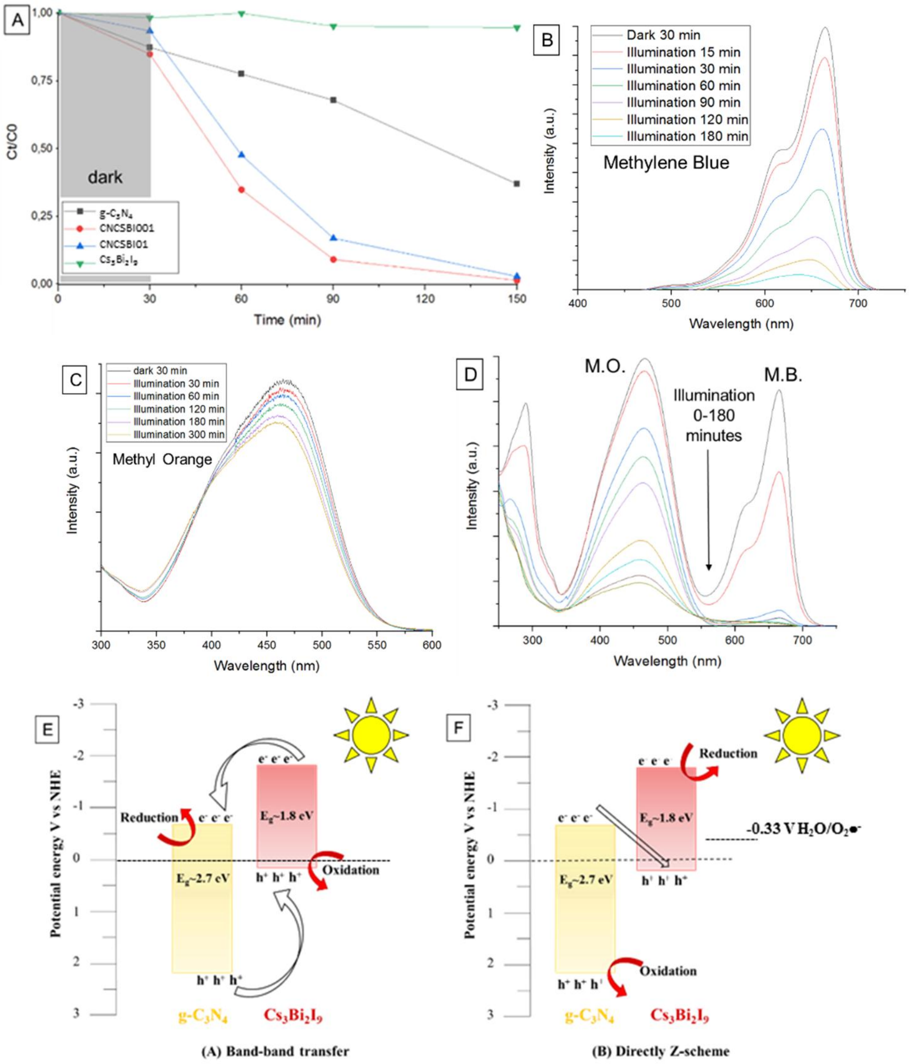

Figure 8: A) *Comparison of RhB photodegradation by g-C_3N_4, CNCSBI001, CNCSBI01 and $Cs_3Bi_2I_9$;* ***B-C)*** *Photodegradation of MB, and MO by CNCSBI001 under LED-visible light irradiation, respectively;* ***D)***

Simultaneous photodegradation of MO and MB over CNCSBI001

A suitable band structure is the key consideration in choosing coupled semiconductors for constructing effective photocatalysts. Based on the previous results the configuration of valence and conduction bands are presented in **Figure 8E-F**. In the composite, the CB position of lead-free perovskite is more negative than that of the carbon-based material, and the graphitic carbon nitride VB has a more negative position. Two types photocatalytic contribution have been considered. If conventional II heterojunction system is considered, it may effectively separate photogenerated electron–hole pairs due to the staggered band structures of the component semiconductors, providing the higher activity respect the bare g-C_3N_4 **Figure 8E**. As an alternative a Z-scheme could be established where the electrons from the CB of g-C_3N_4 combine with the holes from the VB of $Cs_3Bi_2I_9$, acting like scavengers **Figure 8F**. The former double-charge transfer mechanism favors the charge separation, decreasing the potential energy of electrons and holes [46]. This configuration leads to a great reduction in charges recombination in the composite photocatalyst with the respect to the bare components, as shown in the photocurrent and charge-transfer resistance measurements (**Figure 7C-D**). This mechanism is expected to lead to a higher photocatalitic activity [47,48] **Figure 8E**.

A possible pathway of photocatalytic degradation of the organic dyes was proposed. As well known, in a typical photocatalytic process, charge carriers (electrons and holes) can be generated under light illumination (R1). When electrons and holes are separated, they can react with the hydroxyl ions and dissolved oxygen to produce hydroxyl free radicals and superoxide free radicals, as respectively reported in equations R2 and R3. The superoxide radicals may further react with protons and produce H_2O_2 (R4). This reaction can be considered a secondary source for the formation of hydroxyl radicals (R5). The free radicals have a high oxidative capacity, thus and are capable of oxidizing organic compound such as RhB, MB and MO to the complete mineralization with the only release of CO_2 and H_2O (R6). The system of equations is summarized as follows:

Photogeneration of charge carriers

$$\mathrm{CNCSBI001} \xrightarrow{hv} hvb^{+} + ecb^{-} \text{ (R1)}$$

Formation of oxidative species

$$ecb^{-} + O_2 \rightarrow \bullet O_2{}^{-} \text{ (R2)}$$

$$\bullet O_2{}^{-} + \bullet O_2{}^{-} + 2H^{+} \rightarrow O_2 + H_2O_2 \text{ (R3)}$$

$$H_2O_2 + ecb^{-} \rightarrow \bullet OH + OH^{-} \text{ (R4)}$$

Mineralization of RhB

$$RhB + hvb^{+} \rightarrow CO_2 + H_2O \text{ (R5)}$$

Previously, it has been reported that the •O_2^-, h^+, and •OH are in general the major reactive species in photocatalytic oxidation treatments. In order to investigate the mechanism beyond the photocatalytic RhB degradation of the photocatalyst, different scavengers are used to explore the reactive species involved in the process. When the scavengers are added in the reaction solution they are able to selectively remove one of the reactive species. Therefore, based on the change in the photocatalytic efficiency it is possible to determine the active species in the photocatalytic treatment. It is well known that the ammonium oxalate (AO) can be added to remove hole (h^+), iso-propanol (IPA) can be employed to impair the hydroxyl radical (•OH), while p-benzoquinone can be applied to reduce the superoxide radical (•O_2^-) [51–55]. The results of visible-light photocatalytic efficiency on RhB using CNCSBI001 as photocatalyst with various scavengers are shown in **Figure 9A**. When the AO or IPA are added in the reaction solution, the photocatalytic efficiency remains almost invariable. Therefore, holes and hydroxyl radicals appear not to be the major reactive species. On the contrary, after the addition of BQ into the reaction solution, the degradation efficiency of the probe dye remarkably decreases. Thus, based on the previous results, it is clear that •O_2^- is the major reactive specie involved in the photocatalytic reaction system irradiated by LED visible-light. By considering the intrinsic and nonselective character of reactive oxygen radicals we attributed the cleavage of the RhB chromophore structure to attack of the dye, or its radical cations, by superoxide radicals. A possible photoreaction mechanism is summarized in **Figure 9B**. According to previous study, N-deethylation process of RhB can be mainly induced by the produced superoxide radicals in the lead-free based photocatalytic system [56–58].

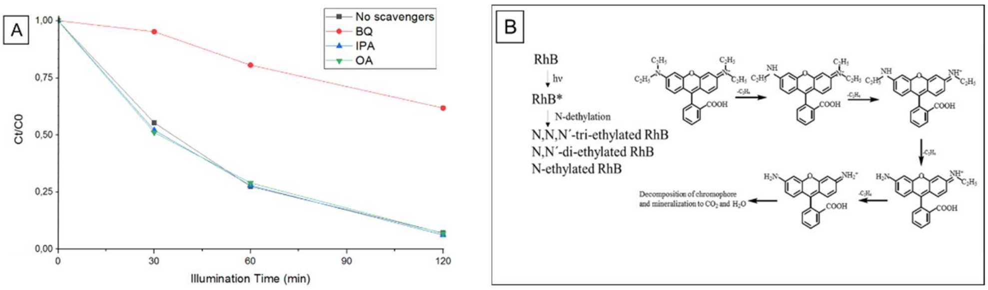

Figure 9: Effect of the addition of different scavengers on the degradation of RhB over CNCSBI001.

In order to investigate the photocatalytic efficiency of the as prepared materials, the formaldehyde concentration during the methanol oxidation was evaluated. The associated fluorescence spectra of the formed DDL are presented in **Figure 10A1**. The measurement shows a continuous increase of formaldehyde concentration with reaction time. The longer irradiation time leads to a higher amount of formaldehyde in the bulk suspension. **Figure 10A2** shows the efficiency achieved after 4 hours of irradiation with three different lamp: solar simulator, LED 406 nm and LED 455 nm. The maximum efficiency was achieved under solar light simulation irradiation due to the wide spectrum of light and higher intensity of the lamp. As previously reported for the organic dyes degradation (R1-R6), free radicals have been considered for their high oxidative capacity as main factors of methanol oxidation. In particular, the photogenerated free radicals are capable of oxidizing methanol by H-atom abstraction (R7). The resulted hydroxymethyl radicals can be further oxidized by the presence of oxygen and they can form formaldehyde (R8) [59].

Methanol oxidation to formaldehyde

$$\bullet OH + CH_3OH \rightarrow H_2O + \bullet CH_2OH \text{ (R7)}$$

$$\bullet CH_2OH + O_2 \rightarrow \bullet O_2CH_2OH \rightarrow HCHO + \bullet {O_2}^- + H^+ \text{ (R8)}$$

The efficiency of the as synthesized material was further investigated for photochemical hydrogen production under solar light irradiation. The photocatalytic hydrogen evolution of the platinized CNCSBI001 was evaluated in methanol:water solution. Under the former conditions, methanol reacts as holes scavenger and the electrons can be transferred to water and produce molecular hydrogen. The experiment was performed up to 6 h of irradiation and samples were withdraw every hour and the amount of evolved hydrogen was measured by gas chromatography at various (**Figure 10B1**). As clearly depicted in the figure, continuous hydrogen production occurs from the beginning of the irradiation period.

Figure 10B2 shows the comparison between pure g-C_3N_4 and the as prepared photocatalyst. The pure g-C_3N_4 sample shows solar-light photocatalytic activity with H_2 evolution reaction (HER) 496.85 µmol $g^{-1}h^{-1}$, attributable to the moderate bandgap and particular electronic structure of g-C_3N_4. After addition with metal halide perovskite, the photocatalytic activity of CNCSBI001 sample was improved of about 46% with a HER of about 920.76 µmol $g^{-1}h^{-1}$. The enhancement of photocatalytic activity was attributed to the improvement of the light absorption and electro-chemical properties of the new designed material.

The consumption of MeOH, as a sacrificial agent, was confirmed by the detection of formaldehyde and a possible mechanism was proposed in the inset of the figure. Finally, in same condition, the hydrogen evolution was further confirmed under visible light irradiation LED 455 nm **Figure 10B3** over 4 hours of illumination. The obtained results confirm the potential of the as prepared material in different photocatalytic applications.

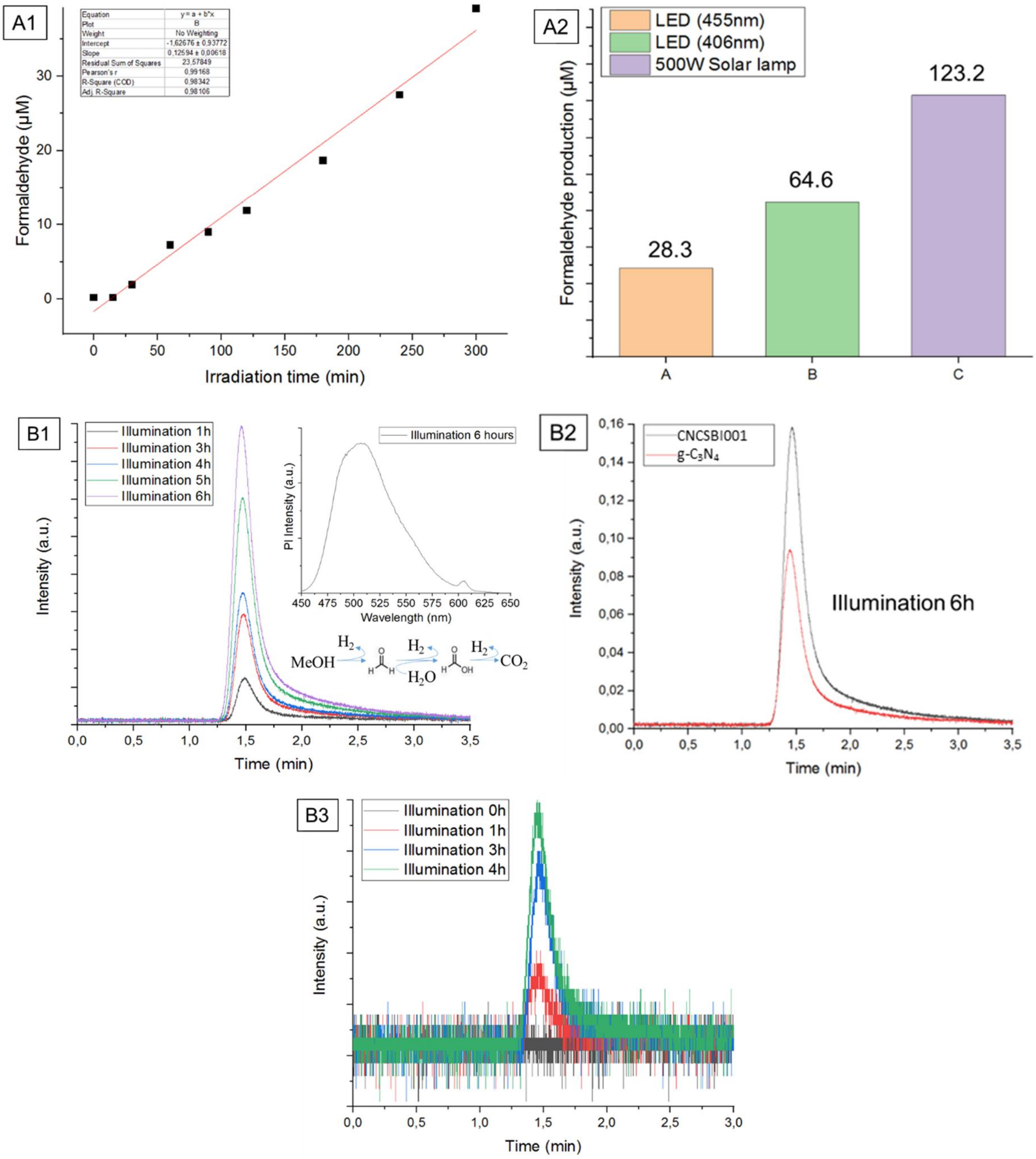

Figure 10: A1) *Oxidation of methanol express as enhance of formaldehyde concentration during visible light photocatalytic experiment under visible light irradiation (455 nm) of CNCSBI001;* ***A2)*** *Comparison of methanol oxidation using three lamps as different energy sources, (inset) Solar energy distribution;* ***B1)*** *Evidence of H_2 evolution, the H_2 peaks produced in GC over 6 h of illumination under solar simulator irradiation;* ***B2)*** *Comparison between activity of pure g-C_3N_4 and the composite photocatalyst;* ***B3)*** *Evidence of H_2 evolution, the H_2 peaks produced in GC over 4 h of illumination under visible light irradiation LED 455 nm.*

3.3 Recycle test

Photocatalytic stability of CNCSBI001 halide perovskite-modified graphitic carbon nitride was confirmed by the recycling tests. The irradiation time of the three subsequent times cycles was performed and the degradation rate change was evaluated. The results shown in **Figure 11A** confirm a negligible decrease in the rate of the process. After the last run, the powder was separated and dried, afterwards, the FTIR spectrum of the samples was collected. As shown in **Figure 11B**, the stability of the as synthesized new photocatalyst was confirmed, no significant or drastic change observed in the existing stretching and bending frequencies of spectrum before and after the degradation. The above achievements illustrated that the prepared material exhibited a good stability and high repeatable ability.

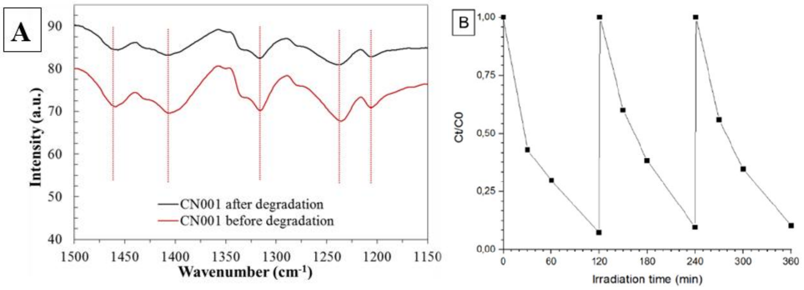

***Figure 11: A)** Cycling tests of photocatalytic degradation RhB in CNCSBI001 under visible light irradiation; **B)** FTIR spectra before and after degradation of RhB under visible-light irradiation*

4. CONCLUSIONS

In recent years, designing visible-light-driven g-C_3N_4 photocatalysts has been rising due to the tunable electronic structure and excellent physicochemical stability it has been shown that they can be excellent candidates in photocatalytic application. In our research, a new composite photocatalyst based on graphitic carbon nitride and lead-free perovskite g-C_3N_4/$Cs_3Bi_2I_9$ was successfully prepared via a facile and reproducible wet chemical method. The accomplishment of the synthesis was evidenced by the morphological characterization of the composite. The as prepared photocatalyst exhibited enhanced photocatalytic performance in the degradation of RhB, MB, MO as well as for the mixture of selected dyes under LED-visible light illumination. The chemical trapping experiments confirmed that, especially for RhB O_2^{-}• was the main active specie in the degradation process under visible light irradiation. Moreover, the as synthesized photocatalyst was found to possess a good stability and recyclability after repeated uses. The as prepared composite was found to be also suitable for visible light degradation of MeOH and H_2 evolution under solar light illumination. The photocatalysts own a remarkably enhanced absorbance in the visible region, due to the narrow band gap of the lead-free perovskite.

The enhance in separation and transport efficiency of photoinduced electron-hole pairs in the photocatalyst were corroborated by photo-electrochemical measurements. The suppressed charge recombination and efficient charge transfer can be ascribed to the heterojunctions formation. The enhanced photocatalytic performance can be attributed to efficient direct scheme heterojunction with a remarkable high redox ability. The results obtained in this work confirm the feasibility of improving the photocatalytic performance of single semiconductors through the formation of composites. Moreover, our work aims to provide important new insights for fabricating composite photocatalysts based on lead-free perovskite material easy to prepare and with suitable properties for photocatalytic applications.

Acknowledgements

Maa-javesitekniikan tuki foundation is gratefully acknowledged for the financial support. This research was supported by Saint-Petersburg State University via a research Grant ID 32706707.

We thank the LNQE (Laboratory of Nano and Quantum Engineering, Hannover, Germany) and the Leibniz University for providing technical equipment and technological knowledge. Moreover, we thank the department of Industrial Engineering of the University of Padova for the providing of materials and support in the syntheses. This research was supported by Saint-Petersburg State University via a research Grant ID 32706707.

REFERENCES

[1] M.R. Hoffmann, S. T. Martin, W. Choi, D. W. Bahnemann, Environmental Applications of Semiconductor Photocatalysis, Chem. Rev. 95 (1995) 69.

[2] A.O.T. Patrocinio, J. Schneider, M.D. França, L.M. Santos, B.P. Caixeta, A.E.H. Machado, D.W. Bahnemann, Charge carrier dynamics and photocatalytic behavior of TiO<inf>2</inf> nanopowders submitted to hydrothermal or conventional heat treatment, RSC Adv. 5 (2015) 70536–70545. doi:10.1039/c5ra13291f.

[3] D. Spasiano, R. Marotta, S. Malato, P. Fernandez-Ibañez, I. Di Somma, Solar photocatalysis: Materials, reactors, some commercial, and pre-industrialized applications. A comprehensive approach, Appl. Catal. B Environ. 170–171 (2015) 90–123. doi:10.1016/j.apcatb.2014.12.050.

[4] T.S. Natarajan, H.C. Bajaj, R.J. Tayade, Enhanced direct sunlight photocatalytic oxidation of methanol using nanocrystalline TiO2 calcined at different temperature, J. Nanoparticle Res. 16 (2014) 2713. doi:10.1007/s11051-014-2713-7.

[5] J. Kou, C. Lu, J. Wang, Y. Chen, Z. Xu, R.S. Varma, Selectivity Enhancement in Heterogeneous Photocatalytic Transformations, Chem. Rev. 117 (2017) 1445–1514. doi:10.1021/acs.chemrev.6b00396.

[6] T.P. Yoon, M.A. Ischay, J. Du, Visible light photocatalysis as a greener approach to photochemical synthesis, Nat. Chem. 2 (2010) 527–532. doi:10.1038/nchem.687.

[7] I.K. Konstantinou, T.A. Albanis, TiO2-assisted photocatalytic degradation of azo dyes in aqueous

solution: Kinetic and mechanistic investigations: A review, Appl. Catal. B Environ. 49 (2004) 1–14. doi:10.1016/j.apcatb.2003.11.010.

[8] F.K. Kessler, Y. Zheng, D. Schwarz, C. Merschjann, W. Schnick, X. Wang, M.J. Bojdys, Functional carbon nitride materials-design strategies for electrochemical devices, Nat. Rev. Mater. 2 (2017). doi:10.1038/natrevmats.2017.30.

[9] X. Liu, M. Wang, S. Zhang, B. Pan, Application potential of carbon nanotubes in water treatment: A review, J. Environ. Sci. (China). 25 (2013) 1263–1280. doi:10.1016/S1001-0742(12)60161-2.

[10] S. Chen, T. Takata, K. Domen, Particulate photocatalysts for overall water splitting, Nat. Rev. Mater. 2 (2017) 1–17. doi:10.1038/natrevmats.2017.50.

[11] J. Ran, W. Guo, H. Wang, B. Zhu, J. Yu, S.Z. Qiao, Metal-Free 2D/2D Phosphorene/g-C 3 N 4 Van der Waals Heterojunction for Highly Enhanced Visible-Light Photocatalytic H 2 Production, Adv. Mater. 30 (2018) 2–7. doi:10.1002/adma.201800128.

[12] J. Joy, J. Mathew, S.C. George, Nanomaterials for photoelectrochemical water splitting – review, Int. J. Hydrogen Energy. 43 (2018) 4804–4817. doi:10.1016/j.ijhydene.2018.01.099.

[13] H. Zhang, L. Zhao, F. Geng, L.H. Guo, B. Wan, Y. Yang, Carbon dots decorated graphitic carbon nitride as an efficient metal-free photocatalyst for phenol degradation, Appl. Catal. B Environ. 180 (2016) 656–662. doi:10.1016/j.apcatb.2015.06.056.

[14] P. Qiu, H. Chen, F. Jiang, Cobalt modified mesoporous graphitic carbon nitride with enhanced visible-light photocatalytic activity, RSC Adv. 4 (2014) 39969–39977. doi:10.1039/c4ra06451h.

[15] S.M. Lam, J.C. Sin, A.R. Mohamed, A review on photocatalytic application of g-C3N4/semiconductor (CNS) nanocomposites towards the erasure of dyeing wastewater, Mater. Sci. Semicond. Process. 47 (2016) 62–84. doi:10.1016/j.mssp.2016.02.019.

[16] S. Kumar, S. Karthikeyan, A. Lee, g-C3N4-Based Nanomaterials for Visible Light-Driven Photocatalysis, Catalysts. 8 (2018) 74. doi:10.3390/catal8020074.

[17] N.G. Park, M. Grätzel, T. Miyasaka, Organic-inorganic halide perovskite photovoltaics: From fundamentals to device architectures, Org. Halide Perovskite Photovoltaics From Fundam. to Device Archit. 3 (2016) 1–366. doi:10.1007/978-3-319-35114-8.

[18] B. Lee, C.C. Stoumpos, N. Zhou, F. Hao, C. Malliakas, C.Y. Yeh, T.J. Marks, M.G. Kanatzidis, R.P.H. Chang, Air-stable molecular semiconducting iodosalts for solar cell applications: Cs2SnI6 as a hole conductor, J. Am. Chem. Soc. 136 (2014) 15379–15385. doi:10.1021/ja508464w.

[19] A. Kojima, K. Teshima, Y. Shirai, T. Miyasaka, Organometal Halide Perovskites as Visible- Light Sensitizers for Photovoltaic Cells, J. Am. Chem. Soc. 131 (2009) 6050–6051. doi:10.1021/ja809598r.

[20] M.A. Pérez-Osorio, R.L. Milot, M.R. Filip, J.B. Patel, L.M. Herz, M.B. Johnston, F. Giustino,

Vibrational Properties of the Organic-Inorganic Halide Perovskite CH3NH3PbI3 from Theory and Experiment: Factor Group Analysis, First-Principles Calculations, and Low-Temperature Infrared Spectra, J. Phys. Chem. C. 119 (2015) 25703–25718. doi:10.1021/acs.jpcc.5b07432.

[21] A. Dualeh, T. Moehl, N. Tétreault, J. Teuscher, P. Gao, M.K. Nazeeruddin, M. Grätzel, Impedance spectroscopic analysis of lead iodide perovskite-sensitized solid-state solar cells, ACS Nano. 8 (2014) 362–373. doi:10.1021/nn404323g.

[22] H. Zai, C. Zhu, H. Xie, Y. Zhao, C. Shi, Z. Chen, X. Ke, M. Sui, C. Chen, J. Hu, Q. Zhang, Y. Gao, H. Zhou, Y. Li, Q. Chen, Congeneric Incorporation of CsPbBr3 Nanocrystals in a Hybrid Perovskite Heterojunction for Photovoltaic Efficiency Enhancement, ACS Energy Lett. 3 (2018) 30–38. doi:10.1021/acsenergylett.7b00925.

[23] Y.F. Xu, M.Z. Yang, B.X. Chen, X.D. Wang, H.Y. Chen, D. Bin Kuang, C.Y. Su, A CsPbBr3 Perovskite Quantum Dot/Graphene Oxide Composite for Photocatalytic CO2 Reduction, J. Am. Chem. Soc. 139 (2017) 5660–5663. doi:10.1021/jacs.7b00489.

[24] N.K. Noel, S.D. Stranks, A. Abate, C. Wehrenfennig, S. Guarnera, A.-A. Haghighirad, A. Sadhanala, G.E. Eperon, S.K. Pathak, M.B. Johnston, A. Petrozza, L.M. Herz, H.J. Snaith, Lead-free organic–inorganic tin halide perovskites for photovoltaic applications, Energy Environ. Sci. 7 (2014) 3061–3068. doi:10.1039/C4EE01076K.

[25] B.W. Park, B. Philippe, X. Zhang, H. Rensmo, G. Boschloo, E.M.J. Johansson, Bismuth Based Hybrid Perovskites A3Bi2I9 (A: Methylammonium or Cesium) for Solar Cell Application, Adv. Mater. 27 (2015) 6806–6813. doi:10.1002/adma.201501978.

[26] C. Cuhadar, S.G. Kim, J.M. Yang, J.Y. Seo, D. Lee, N.G. Park, All-Inorganic Bismuth Halide Perovskite-like Materials A3Bi2I9 and A3Bi1.8Na0.2I8.6 (A = Rb and Cs) for Low-Voltage Switching Resistive Memory, ACS Appl. Mater. Interfaces. 10 (2018) 29741–29749. doi:10.1021/acsami.8b07103.

[27] M. Ou, W. Tu, S. Yin, W. Xing, S. Wu, H. Wang, S. Wan, Q. Zhong, R. Xu, Amino-Assisted Anchoring of CsPbBr3 Perovskite Quantum Dots on Porous g-C3N4 for Enhanced Photocatalytic CO2 Reduction, Angew. Chemie - Int. Ed. 57 (2018) 13570–13574. doi:10.1002/anie.201808930.

[28] L. Shi, T. Wang, H. Zhang, K. Chang, J. Ye, Electrostatic Self-Assembly of Nanosized Carbon Nitride Nanosheet onto a Zirconium Metal-Organic Framework for Enhanced Photocatalytic CO<inf>2</inf> Reduction, Adv. Funct. Mater. 25 (2015) 5360–5367. doi:10.1002/adfm.201502253.

[29] W. Tu, Y. Xu, J. Wang, B. Zhang, T. Zhou, S. Yin, S. Wu, C. Li, Y. Huang, Y. Zhou, Z. Zou, J. Robertson, M. Kraft, R. Xu, Investigating the Role of Tunable Nitrogen Vacancies in Graphitic Carbon Nitride Nanosheets for Efficient Visible-Light-Driven H2 Evolution and CO2 Reduction,

ACS Sustain. Chem. Eng. 5 (2017) 7260–7268. doi:10.1021/acssuschemeng.7b01477.

[30] X. Li, Y. Wang, H. Sun, H. Zeng, Amino-Mediated Anchoring Perovskite Quantum Dots for Stable and Low-Threshold Random Lasing, Adv. Mater. 29 (2017) 1–9. doi:10.1002/adma.201701185.

[31] J. De Roo, M. Ibáñez, P. Geiregat, G. Nedelcu, W. Walravens, J. Maes, J.C. Martins, I. Van Driessche, M. V. Kovalenko, Z. Hens, Highly Dynamic Ligand Binding and Light Absorption Coefficient of Cesium Lead Bromide Perovskite Nanocrystals, ACS Nano. 10 (2016) 2071–2081. doi:10.1021/acsnano.5b06295.

[32] K. Sharma, V. Dutta, S. Sharma, P. Raizada, A. Hosseini-Bandegharaei, P. Thakur, P. Singh, Recent advances in enhanced photocatalytic activity of bismuth oxyhalides for efficient photocatalysis of organic pollutants in water: A review, J. Ind. Eng. Chem. 78 (2019) 1–20. doi:10.1016/j.jiec.2019.06.022.

[33] M. Zhang, J. Xu, R. Zong, Y. Zhu, Enhancement of visible light photocatalytic activities via porous structure of g-C3N4, Appl. Catal. B Environ. 147 (2014) 229–235. doi:10.1016/j.apcatb.2013.09.002.

[34] S.C. Yan, Z.S. Li, Z.G. Zou, Photodegradation performance of g-C3N4 fabricated by directly heating melamine, Langmuir. 25 (2009) 10397–10401. doi:10.1021/la900923z.

[35] N. Tian, H. Huang, Y. He, Y. Guo, Y. Zhang, Novel g-C3N4/BiIO4heterojunction photocatalysts: Synthesis, characterization and enhanced visible-light-responsive photocatalytic activity, RSC Adv. 4 (2014) 42716–42722. doi:10.1039/c4ra05917d.

[36] J. Pal, A. Bhunia, S. Chakraborty, S. Manna, S. Das, A. Dewan, S. Datta, A. Nag, Synthesis and Optical Properties of Colloidal M3Bi2I9 (M=Cs, Rb) Perovskite Nanocrystals, J. Phys. Chem. C. 122 (2018) acs.jpcc.8b03542. doi:10.1021/acs.jpcc.8b03542.

[37] C.H.R. C-h, Infrared absorption data for some functional groups not listed in the preceding table are given below . Most of the absorptions cited are associated with stretching, 1720 (1820).

[38] J.C. Bailar, N. Ch, INFRARED SPECTRA OF, 36 (1974).

[39] Y. Cai, J. Lv, J. Feng, Spectral Characterization of Four Kinds of Biodegradable Plastics: Poly (Lactic Acid), Poly (Butylenes Adipate-Co-Terephthalate), Poly (Hydroxybutyrate-Co-Hydroxyvalerate) and Poly (Butylenes Succinate) with FTIR and Raman Spectroscopy, J. Polym. Environ. 21 (2013) 108–114. doi:10.1007/s10924-012-0534-2.

[40] A. Menikh, MOLECULAR STRUCTURE Spectroscopic and electrochemical studies of N , N â€™ - bis (decamethylcarboxylic) -3 , 4 , 9 , 10-perylene-bis (dicarboxyimide), 403 (1997) 189–197.

[41] S. Krzemińska, L. Lipińska, M. Woluntarski, M. Oleksy, C. Ślusarczyk, W. Biniaś, A. Smejda-Krzewicka, Hybrid XNBR composites with carbon and aluminosilicate nanofillers, 2019. doi:10.1007/s00289-019-02825-9.

[42] Y. Joon, J. Joon, Y. Il, J. Kook, H. Na, J. Kim, S. Bin, Oxygen functional groups and electrochemical capacitive behavior of incompletely reduced graphene oxides as a thin-film electrode of supercapacitor, Electrochim. Acta. 116 (2014) 118–128. doi:10.1016/j.electacta.2013.11.040.

[43] P. Shandilya, D. Mittal, M. Soni, P. Raizada, A. Hosseini-Bandegharaei, A.K. Saini, P. Singh, Fabrication of fluorine doped graphene and SmVO4 based dispersed and adsorptive photocatalyst for abatement of phenolic compounds from water and bacterial disinfection, J. Clean. Prod. 203 (2018) 386–399. doi:10.1016/j.jclepro.2018.08.271.

[44] Y. Yang, W. Guo, Y. Guo, Y. Zhao, X. Yuan, Y. Guo, Fabrication of Z-scheme plasmonic photocatalyst Ag@AgBr/g-C3N4 with enhanced visible-light photocatalytic activity, J. Hazard. Mater. 271 (2014) 150–159. doi:10.1016/j.jhazmat.2014.02.023.

[45] A.J. Lehner, D.H. Fabini, H.A. Evans, C.A. Hébert, S.R. Smock, J. Hu, H. Wang, J.W. Zwanziger, M.L. Chabinyc, R. Seshadri, Crystal and Electronic Structures of Complex Bismuth Iodides A3Bi2I9(A = K, Rb, Cs) Related to Perovskite: Aiding the Rational Design of Photovoltaics, Chem. Mater. 27 (2015) 7137–7148. doi:10.1021/acs.chemmater.5b03147.

[46] M. Aguirre, Matias; Zhou, Ruixin; Eugene, Alexis; Guzman, Marcelo; Grela, Cu2O/TiO2 heterostructure for CO2 reduction through a drect Z-scheme: Protecting Cu2O from photocorrosion, Appl. Catal. B Environ. 217 (2017) 485–493. doi:10.1016/j.apcatb.2017.05.058.

[47] P. Raizada, A. Sudhaik, P. Singh, A. Hosseini-Bandegharaei, P. Thakur, Converting type II AgBr/VO into ternary Z scheme photocatalyst via coupling with phosphorus doped g-C3N4 for enhanced photocatalytic activity, Sep. Purif. Technol. 227 (2019) 115692. doi:10.1016/j.seppur.2019.115692.

[48] P. Raizada, A. Sudhaik, P. Singh, P. Shandilya, V.K. Gupta, A. Hosseini-Bandegharaei, S. Agrawal, Ag 3 PO 4 modified phosphorus and sulphur co-doped graphitic carbon nitride as a direct Z-scheme photocatalyst for 2, 4-dimethyl phenol degradation, J. Photochem. Photobiol. A Chem. 374 (2019) 22–35. doi:10.1016/j.jphotochem.2019.01.015.

[49] P. Wongkalasin, S. Chavadej, T. Sreethawong, Photocatalytic degradation of mixed azo dyes in aqueous wastewater using mesoporous-assembled TiO2 nanocrystal synthesized by a modified sol-gel process, Colloids Surfaces A Physicochem. Eng. Asp. 384 (2011) 519–528. doi:10.1016/j.colsurfa.2011.05.022.

[50] A.K. Gupta, A. Pal, C. Sahoo, Photocatalytic degradation of a mixture of Crystal Violet (Basic Violet 3) and Methyl Red dye in aqueous suspensions using Ag+ doped TiO2, Dye. Pigment. 69 (2006) 224–232. doi:10.1016/j.dyepig.2005.04.001.

[51] S. Chen, Y. Hu, S. Meng, X. Fu, Study on the separation mechanisms of photogenerated electrons and holes for composite photocatalysts g-C3N4-WO3, Appl. Catal. B Environ. 150–151 (2014)

564–573. doi:10.1016/j.apcatb.2013.12.053.

[52] X. Ding, X. Song, P. Li, Z. Ai, L. Zhang, Efficient visible light driven photocatalytic removal of NO with aerosol flow synthesized B, N-codoped TiO2 hollow spheres, J. Hazard. Mater. 190 (2011) 604–612. doi:10.1016/j.jhazmat.2011.03.099.

[53] Z. He, Y. Shi, C. Gao, L. Wen, J. Chen, S. Song, BiOCl/BiVO\textsubscript{4} p–n Heterojunction with Enhanced Photocatalytic Activity under Visible-Light Irradiation, J. Phys. Chem. C. 118 (2014) 389–398. doi:10.1021/jp409598s.

[54] M. Mousavi, A. Habibi-Yangjeh, Magnetically separable ternary g-C3N4/Fe3O4/BiOI nanocomposites: Novel visible-light-driven photocatalysts based on graphitic carbon nitride, J. Colloid Interface Sci. 465 (2016) 83–92. doi:10.1016/j.jcis.2015.11.057.

[55] J. Wang, L. Tang, G. Zeng, Y. Deng, Y. Liu, L. Wang, Y. Zhou, Z. Guo, J. Wang, C. Zhang, Applied Catalysis B : Environmental Atomic scale g-C 3 N 4 / Bi 2 WO 6 2D / 2D heterojunction with enhanced photocatalytic degradation of ibuprofen under visible light irradiation, "Applied Catal. B, Environ. 209 (2017) 285–294. doi:10.1016/j.apcatb.2017.03.019.

[56] J. Jin, Q. Liang, C. Ding, Z. Li, S. Xu, Simultaneous synthesis-immobilization of Ag nanoparticles functionalized 2D g-C3N4nanosheets with improved photocatalytic activity, J. Alloys Compd. 691 (2017) 763–771. doi:10.1016/j.jallcom.2016.08.302.

[57] H. Liang, S. Liu, H. Zhang, X. Wang, J. Wang, New insight into the selective photocatalytic oxidation of RhB through a strategy of modulating radical generation, RSC Adv. 8 (2018) 13625–13634. doi:10.1039/c8ra01810c.

[58] X. Hu, T. Mohamood, W. Ma, C. Chen, J. Zhao, Oxidative decomposition of rhodamine B dye in the presence of VO 2+ and/or Pt(IV) under visible light irradiation: N-deethylation, chromophore cleavage, and mineralization, J. Phys. Chem. B. 110 (2006) 26012–26018. doi:10.1021/jp063588q.

[59] C. yi Wang, J. Rabani, D.W. Bahnemann, J.K. Dohrmann, Photonic efficiency and quantum yield of formaldehyde formation from methanol in the presence of various TiO2photocatalysts, J. Photochem. Photobiol. A Chem. 148 (2002) 169–176. doi:10.1016/S1010-6030(02)00087-4.